Computational Condensed Matter 21 (2019) e00404

Contents lists available at ScienceDirect

Computational Condensed Matter

journal homepage: http://ees.elsevier.com/cocom/default.asp

Absorption and diffusion of lithium on layered InSe

Xiuying Zhang [a], Sibai Li [b], Jingzhen Li [a], Meng Ye [c], Zhigang Song [d], Shan Jin [e], Bowen Shi [a], Yuanyuan Pan [a], Jiahuan Yan [a], Yangyang Wang [f, ****], Jiaxin Zheng [b, ***], Feng Pan [b, **], Jing Lu [a, g, *]

[a] State Key Laboratory for Mesoscopic Physics and Department of Physics, Peking University, Beijing, 100871, China
[b] School of Advanced Materials, Peking University, Shenzhen Graduate School, Shenzhen, 518055, China
[c] State Key Laboratory for Superlattices and Microstructures, Institute of Semiconductors, Chinese Academy of Sciences, Beijing, 100083, China
[d] Department of Engineering, University of Cambridge, JJ Thomson Avenue, CB3 0FA, Cambridge, UK
[e] School of Nano Technology and Nano Bionics, University of Science and Technology of China, Suzhou, 215123, Jiangsu, China
[f] Nanophotonics and Optoelectronics Research Center, Qian Xuesen Laboratory of Space Technology, China Academy of Space Technology, Beijing, 100094, China
[g] Collaborative Innovation Center of Quantum Matter, Beijing, 100871, China

ARTICLE INFO

Article history:
Received 25 January 2019
Received in revised form
20 April 2019
Accepted 23 May 2019

Keywords:
Indium selenide
Li-ion absorption
Li-ion diffusion
Density functional theory

ABSTRACT

Two-dimensional indium selenide (InSe) is attracting much recent attention due to its high electron mobility. Using *ab initio* calculations, we systematically investigate the absorption and diffusion of lithium (Li) ion inside layered InSe. We find that firstly the binding energy absolute values for Li-ion absorbed on bulk and monolayer (ML) InSe range from 0.43 to 1.61 eV, which are large enough to stabilize Li–InSe systems. The absolute value of the binding energy is also approximately monotonically decreased with the increasing of Li-ion density. Secondly, the structure of InSe isn't deformed much by the insertion of Li, and the largest crystalline size change is only 4.68%, indicating the robustness of InSe against the insertion of Li ions. Thirdly, the diffusion barriers heights for Li ions diffusion inside bulk and ML InSe are 0.02–0.06 eV and 0.18–0.24 eV, respectively, and the diffusion barrier heights monotonically decrease with the increasing of Li-ion density. Finally, after the absorption of Li ions, InSe transforms from semiconductor to metal, rendering Li–InSe systems as good electrical conductors.

1. Introduction

Layered materials have attracted significant attentions due to their special structure advantages, which helps them give low diffusion barrier height for ions such as Li-ion. For example, the diffusion barrier height is only 0.05 and 0.08 eV for Li-ions diffusion in bulk black phosphorus and on monolayer (ML) black phosphorene, respectively [1]. ML borophene exhibits much high diffusion velocity for metal ions with the diffusion barrier height of 0.025, 0.003, 0.028, 0.440 eV for Li, Na, Mg, Ca ions, respectively [2]. Futhermore, transition metal carbides or nitrides (MXenes), a new kind of two dimensional (2D) materials, also exhibit much low diffusion barrier height (0.015–0.07 eV) [3,4]. Besides, layered materials can trap metal ions diffusion into two dimensions and significantly shorten the diffusion path [5,6], enabling faster ion diffusion. The special groove structure can even trap metal ions diffusion into one dimension, and the diffusion path can be further shortened and the diffusion velocity can be also accelerated a lot [1].

Indium selenide (InSe) is a member of layered material family with honeycomb lattice structures in each of its layers as shown in Fig. 1(a–c) [7–10]. More recently, 2D InSe has been synthesized in experiments from mechanical exfoliation and exhibited promising characteristics for electronic, optoelectronic, and thermal applications with much high electron mobility (10^3 $cm^2/V{\cdot}s$ at room temperature), combined with a high thermal stability up to 660 °C [11–18]. The specific puckered honeycomb structure could provide excellent Li-ion passage where Li ions could move straight forward

* Corresponding author. State Key Laboratory for Mesoscopic Physics and Department of Physics, Peking University, Beijing, 100871, China.
** Corresponding author.
*** Corresponding author.
**** Corresponding author.
E-mail addresses: wangyangyang@qxslab.cn (Y. Wang), zhengjx@pkusz.edu.cn (J. Zheng), panfeng@pkusz.edu.cn (F. Pan), jinglu@pku.edu.cn (J. Lu).

https://doi.org/10.1016/j.cocom.2019.e00404
2352-2143/

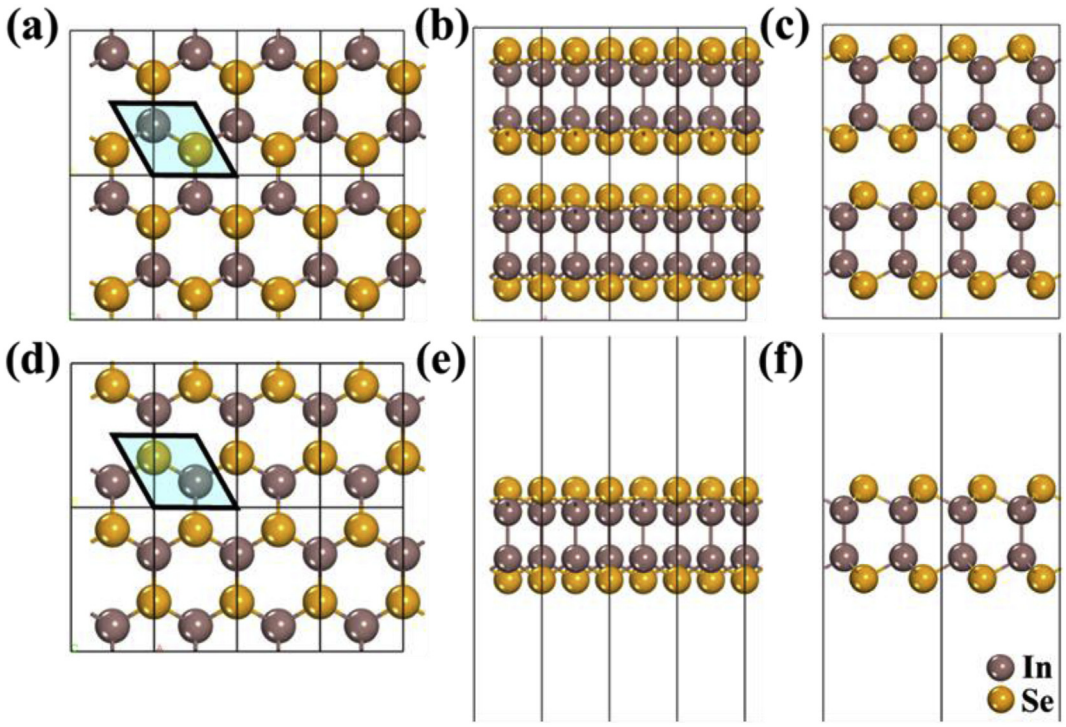

Fig. 1. Structure models of layered InSe. (a–c) Top and side view of bulk InSe; (d–f) same as (a–c) but for ML InSe. The green rhombuses represent the primitive cell of bulk (a) and ML (d) InSe. The yellow and brown ball represent Se and In atom, respectively. (For interpretation of the references to colour in this figure legend, the reader is referred to the Web version of this article.)

along the groove direction [6,19], and thus significantly shorten the diffusion pathway [5,6]. As a result, the diffusion velocity of Li ions can be accelerated.

In this article, first principles calculation based on density functional theory (DFT) is used to investigate the absorption and diffusion processes of Li ions in both bulk and ML InSe. Our study indicates that Li ions have stable absorption with both bulk and ML InSe with minus binding energies ranging from −0.43 to −1.61 eV. Li ions move only along the groove direction in InSe, and the migration barrier heights for Li ions diffusion in both bulk and ML InSe decrease as the Li density increases. The barriers in bulk InSe range from 0.027 to 0.054 eV and these on the surface of ML InSe range from 0.182 to 0.236 eV, which are quite low compared with other materials. Our work provides directions for searching for electrode material with high ion diffusion velocity.

1.1. Computational details

The geometry optimization and the electronic property calculations are implemented in the Atomistix ToolKit (ATK) 2016 package [20]. The electron exchange-correlation interactions are treated using generalized gradient approximation (GGA) in the scheme of Perdew-Burke-Ernzerhof (PBE) [21]. The SG15 collection of optimized norm-conserving Vanderbilt (ONCV) pseudopotentials and ultra-high basis set are used to optimize the structures and study the electronic properties, and the convergence criteria of electron self-consistent lop is set to 10^{-6} eV. Atomic relaxation is performed until all the forces on each atom are smaller than 0.01 eV/Å. A vacuum layer of at least 15 Å is added to avoid image-image interaction during the calculations of ML InSe. A *k*-mesh density of 0.02 $Å^{-1}$ under the Monkhorst-Pack method [22] is sampled in the Brillouin zone. The binding energy (E_b) can be defined as

$$E_b = \left(E_{complex} - E_{InSe} - nE_{Li}\right)/n$$

where $E_{complex}$, E_{InSe}, and E_{Li} are the energies of Li-ion absorbed InSe, ML or bulk InSe, and metallic Li, respectively, and n is the number of Li ions absorbed on InSe. In such a definition, a larger absolute minus value of E_b corresponds to a more energetically favorable reaction.

The calculation of Li-ion diffusion barriers is also implemented in the Atomistix ToolKit (ATK) 2016 package that is performed through the minimum energy path profiling using the climbing image nudged elastic band (CI-NEB) method [23,24]. Fritz-Haber Institute (FHI) exchange-correlation functional with double-ζ plus polarization (DZP) basis set is used to calculate the reaction path, because the SG-15 pseudopotential with ultra-high basis set is extremely time consuming. The convergence criteria and electron exchange-correlation interactions are treated in the same way as in the process of geometry optimization and electronic property calculations.

The van der Waals correction is tested in our calculations. The vdW-D2/3 corrections are the only usable vdW corrections in ATK 2016 package, and we used vdW-D3 correction here. We find that the correction has almost no influence to our results. For example, the difference between the binding energy for lithiuated bulk InSe with vdW-D3 correction and that without vdW-D3 correction is very small (about 18 meV/atom). Besides, the time that the calculation with vdW-D3 correction takes would be about twice as much as that the calculation without vdW-D3 correction takes. So, the vdW-D3 correction is not used in this work.

2. Results and discussions

2.1. Absorption of Li ions

We firstly explore the most favorable binding site for Li ions in

bulk and ML InSe. Fig. 2 shows the structures after the absorption of Li ions on bulk (a-d) and ML (e-h) InSe. We only consider the stage II structures [25] for bulk InSe where one empty layer exists between each Li-ion absorbed layers as shown in Fig. 2(a–d). The purple circles in Fig. 2 (b) indicate the location of Li ions. We considered two high-symmetry absorption sites for Li ions in bulk InSe (Fig. S1). One is on the hollow site above the center of the hexagon (H site) (Fig. S1(a)), and the corresponding E_b is −0.81 eV; the other is upon a Se-atom and also under an In-atom of the other layer of InSe (T site) (Fig. S1(b)), and the corresponding E_b is −0.99 eV. The binding energy at the T site is smaller than that at the H site, and thus, the T site is more stable than the H site for Li ions absorption in bulk InSe. We considered three high-symmetry absorption sites on ML InSe surface (Fig. S2). The first one is on the hollow site above the center of the hexagon (H site) (Fig. S2(a)), and the corresponding E_b is −0.49 eV; the second one is on the top of a Se-atom (T_{Se} site) (Fig. S2(b)), and after fully relaxation, it moves to the H site, indicating the instability of T_{Se} site; the third one is on the top of an In-atom (T_{In} site) (Fig. S2(c)) and the corresponding E_b is −0.24 eV. Li ions have the smallest binding energy at the H site and thus, the most stable site for Li ions absorption on ML InSe is the H site.

Through putting one Li-ion at the most stable binding site (T_{In} site for bulk and H site for ML InSe) in a 5×1, 4×1, 3×1, 2×1, 1×1 supercell, and a primitive cell (Fig. 3), a number of configurations with stoichiometry of $Li_x(InSe)_{4(2)}$ (4 for bulk, 2 for ML) ($x = 0.1$, 0.125, 0.167, 0.25, 0.5, and 1, respectively) are constructed. At $x = 0.1$, 0.125, 0.167, 0.25, 0.5, and 1 for both bulk and ML InSe, the distance between two nearest Li ions is about 20.6, 16.5, 12.4, 8.3, 4.0, and 4.1 Å, respectively in the x direction. The distance is about 7.1 Å in the y direction at $x = 0.1$, 0.125, 0.167, 0.25, and 0.5, and about 4.1 Å at $x = 1$. The distance in the z direction for bulk InSe is about 17.8 Å at all the Li-ion densities. During the geometrical relaxation, the lattice parameters are also optimized. The largest in-plane lattice change after Li ions loading on bulk InSe is 2.98% and on ML InSe is 2.19% during the lithiuation process (Table 1), although the largest lattice change happens in the out-of-plane direction for the bulk InSe, which is 4.68%. The small lattice change means that InSe is robust against Li-ion insertion and doesn't suffer from large structural changes. The distance between the Li ions and the adjacent In/Se-atom upon/under the Li ions is about 3.0/2.5 Å for Li ions absorption in bulk InSe at all the studied Li-ion densities. The distance from the Li ions to InSe surface is about 1.1 Å for Li ions absorption on the surface of ML InSe at all the studied Li-ion densities.

The binding energies for Li ions absorbed on bulk and ML InSe are all minus values at all the Li-ion densities (Fig. 4). Such minus binding energies means that the Li–InSe system is stable and the binding process of Li ions on InSe is an exothermic process. The absolute values of the binding energies for Li ions inserted in bulk InSe monotonically decrease with the increasing of Li density and range between 1.61 eV at $x = 0.1$ and 0.62 eV at $x = 1$. For Li ions loading on the surface of ML InSe, the absolute value of binding energy also approximately monotonically decreases with the increasing Li-ion density and ranges between 0.96 eV at $x = 0.1$ and 0.43 eV at $x = 1$. However, there is an exception for ML InSe at $x = 0.5$; the absolute value of binding energy is increased to 0.68 eV at this density from 0.49 eV at $x = 0.25$. The enhancement bonding is mainly induced by the structure deformation of ML InSe on the state $Li_{0.5}(InSe)_2$ as displayed in Fig. 3. The original perfect honeycomb lattice structure is deformed, with some of the In–Se bonds broken on the state $Li_{0.5}(InSe)_2$. The Se atoms released from the broken In–Se bonds, could absorb more Li ions, resulting in the enhanced bonding of Li-ion on ML InSe.

The absolute values of the binding energies are larger than many other values for Li ions absorbed on layer materials. For example, the binding energies for the Li ions absorption on few layer graphene and graphite are about −0.03 eV [26], and those for Li ions absorption on silicone sulfide are about −0.38 eV and on ML SiS with different phase are −0.4 to −0.51 eV [27,28]. According to the thermodynamic theory, the larger the energy difference between the reactant and the product, the faster the reaction process, and thus a more rapid absorption process of the Li ions. Bulk InSe has a stronger binding (−0.62 to −1.61 eV) with Li ions than that of ML (−0.43 to −0.96 eV) at the same x, which means that bulk InSe has a faster Li loading process than ML does.

2.2. Electronic properties of Li/InSe configuration

The band structures and the partial density of states (PDOS) of

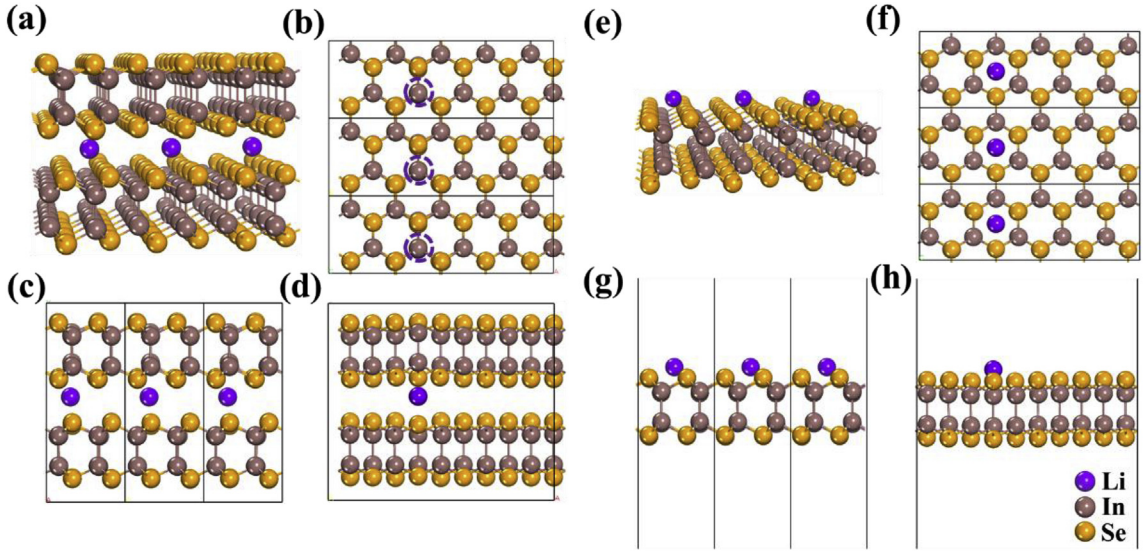

Fig. 2. Structure model of fully optimized Li-ion-absorbed InSe. (a) General view, (b) top view, and (c,d) side view of bulk InSe; (e–h) Same as (a–d) but for ML InSe. The yellow, brown, and purple balls represent Se, In, and Li-atom, respectively. (For interpretation of the references to colour in this figure legend, the reader is referred to the Web version of this article.)

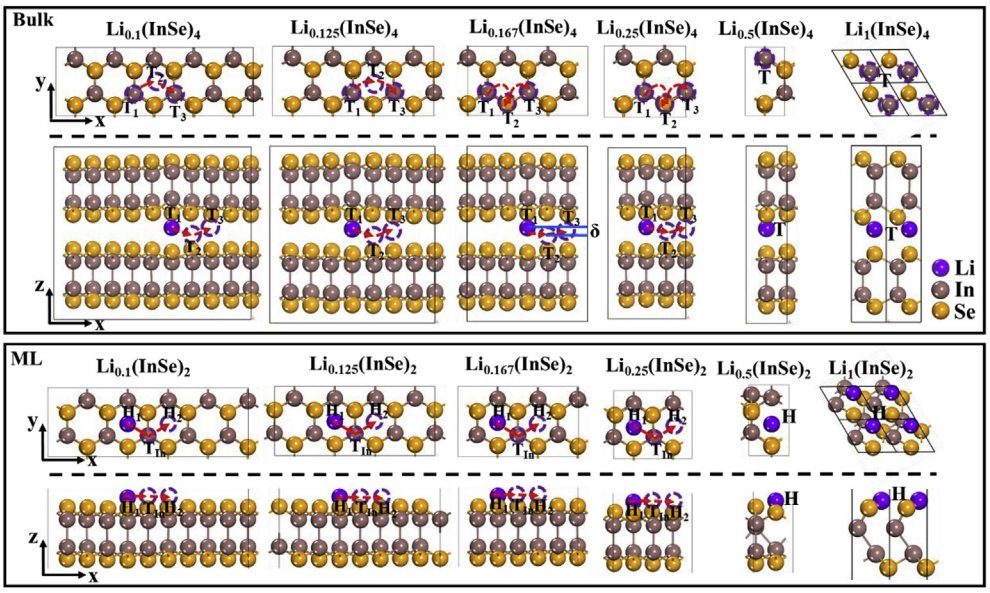

Fig. 3. Top and side views of the Li-ion diffusion pathway ($T_1 \rightarrow T_2 \rightarrow T_3$ for bulk and $H_1 \rightarrow T_{In} \rightarrow H_2$ for ML) for different lithium absorbed density of bulk and ML InSe ($Li_x(InSe)_{4(2)}$). The yellow, brown, and purple balls represent Se, In, and Li-atom, respectively. (For interpretation of the references to colour in this figure legend, the reader is referred to the Web version of this article.)

Table 1
The lattice parameter (x, y, z) of original and the lithiuated bulk and ML InSe. Δx, Δy, and Δz represent the lattice parameter changes corresponding to the original bulk and ML InSe during lithiuation process.

bulk	InSe	$Li_{0.1}(InSe)_4$	$Li_{0.125}(InSe)_4$	$Li_{0.167}(InSe)_4$	$Li_{0.25}(InSe)_4$	$Li_{0.5}(InSe)_4$	$Li_1(InSe)_4$
x	4.06	20.62	16.51	12.38	8.26	4.15	4.15
y	7.03	7.13	7.14	7.15	7.17	7.16	7.19
z	17.43	18.00	17.67	18.03	18.11	17.91	18.25
Δx		1.60%	1.67%	1.66%	1.75%	2.27%	2.27%
Δy		1.37%	1.62%	1.71%	1.99%	1.82%	2.27%
Δz		3.22%	1.35%	3.44%	3.89%	2.73%	4.68%
ML	InSe	$Li_{0.1}(InSe)_2$	$Li_{0.125}(InSe)_2$	$Li_{0.167}(InSe)_2$	$Li_{0.25}(InSe)_2$	$Li_{0.5}(InSe)_2$	$Li_1(InSe)_2$
x	4.08	20.65	16.53	12.40	8.34	4.07	4.10
y	7.07	7.15	7.16	7.21	7.21	7.23	7.11
Δx		1.13%	1.20%	1.18%	2.03%	−0.34%	0.47%
Δy		1.05%	1.24%	1.88%	1.91%	2.19%	0.48%

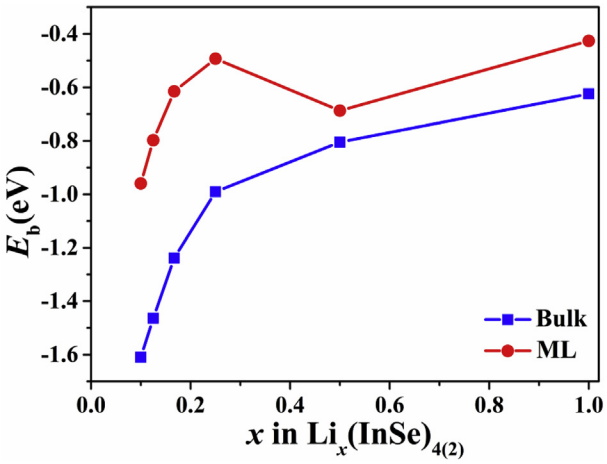

Fig. 4. Binding energy of Li-ion on bulk (black) and ML (red) InSe as a function of Li density x in $Li_x(InSe)_{4(2)}$. (For interpretation of the references to colour in this figure legend, the reader is referred to the Web version of this article.)

pristine and Li absorbed bulk (ML) InSe are presented in Fig. 5 (Fig. 6). Both bulk and ML pristine InSe are semiconductors, with a band gap of 0.57 and 1.37 eV, respectively (Figs. 5(a) and Fig. 6(a)). After absorption of Li ions, the band structures of InSe are nearly intact, but the Fermi level is shifted upward into the conduction band (Figs. 5(d) and Fig. 6(d)), making InSe transform to a metallic state. The transition from semiconductor to metal after absorption of Li ions is also observed in other lithiated semiconductors such as phosphorene and VS_2 [6,29].

We compare the band structure and DOS of the lithiated bulk (Fig. S3) and ML (Fig. S4) InSe calculated using FHI pseudopotential with DZP basis set with those calculated using SG-15 pseudopotential with ultra-high basis set. Both the band structure and DOS with the two methods show that the Fermi level moves upward into the conduction band after the absorption of Li-ions for both bulk and ML InSe. But the band structure of SG-15 method shows similar band dispersion with that in other works [12,30]. For example, the conduction band minimum is located at the Γ point in the band structure with SG-15 method, the same as the results in other works. But the band structure with DZP method shows that the conduction band minimum is located at around the M point.

The band gaps for pristine bulk and ML InSe are indeed

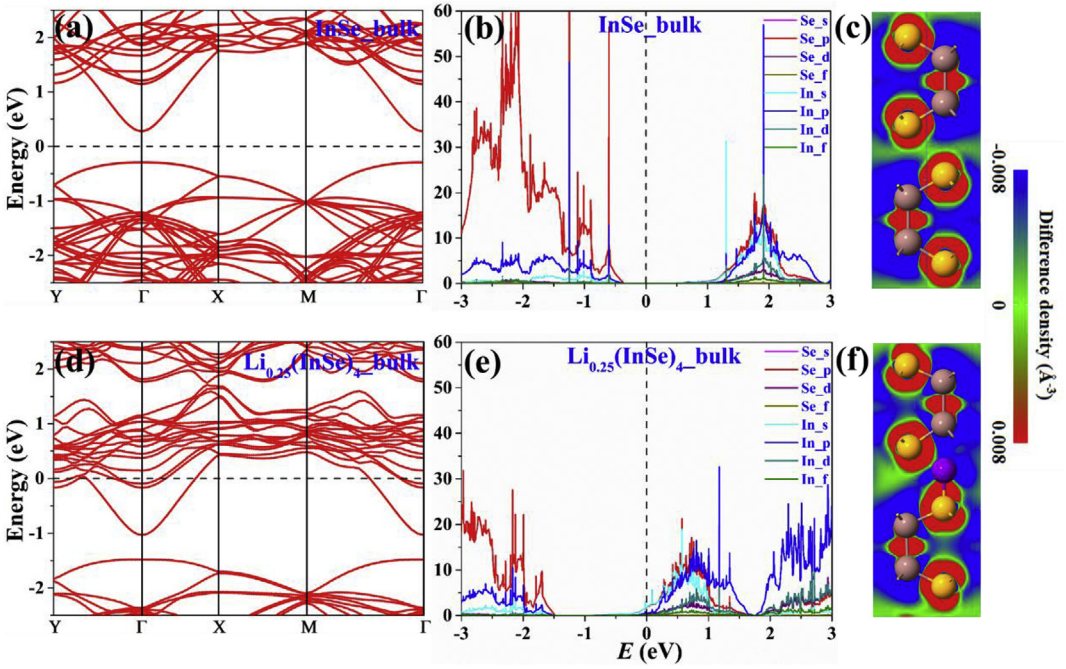

Fig. 5. (a) Electronic band structures, (b) total density of states and projected density of states, and (c) differential electrons potential of pristine bulk InSe. (d–f) Same as (a–c) but for lithuated bulk InSe $Li_{0.1}(InSe)_4$.

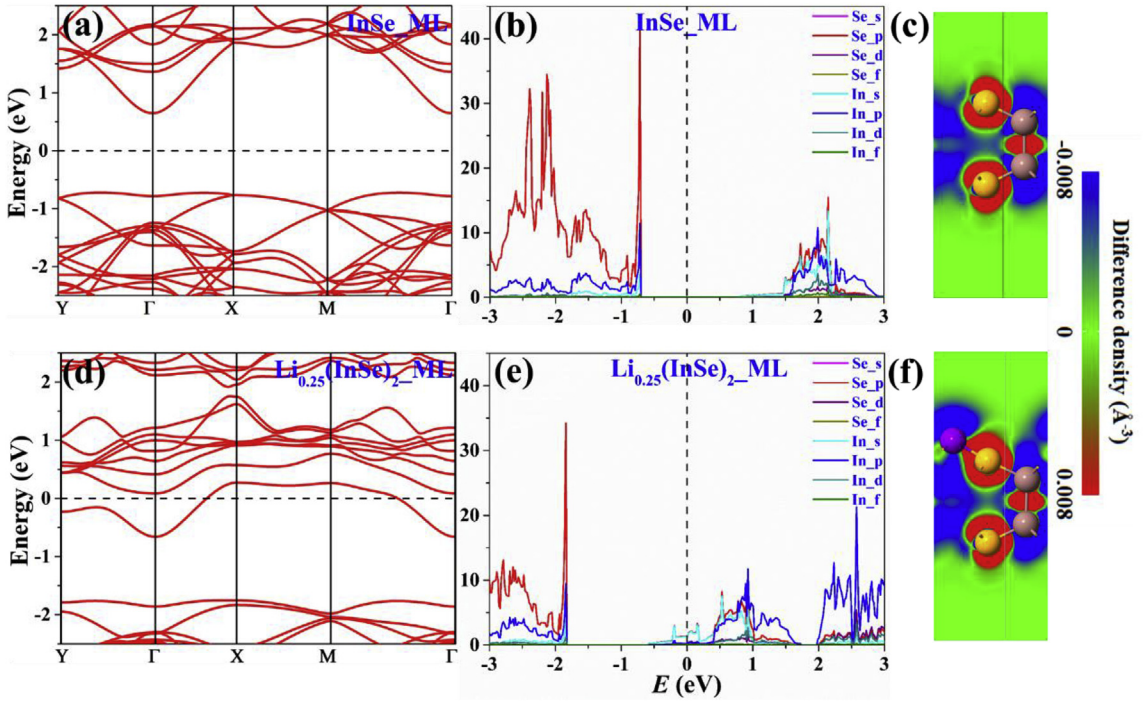

Fig. 6. (a) Electronic band structures, (b) total density of states and projected density of states, and (c) differential electrons potential of pristine ML InSe. (d–f) Same as (a–c) but for lithuated ML InSe $Li_{0.1}(InSe)_2$.

underestimated with DFT-PBE method. But after absorption of Li ions, InSe is highly doped, and for a heavily doped semiconductor, the screening effect between electrons is increased, the interaction between the electrons is greatly reduced, and therefore the single particle approximation on which the DFT-PBE method is based is a good approximation to estimate the bandgaps of a heavily doped system [31,32].

For example, the measured transport gaps, which reflect the band gaps of a degenerately doped system, for ML, bilayer, and trilayer black phosphorene (BP) are 1.00, 0.71, and 0.61 eV, respectively [33], and the respective calculated transport gaps with DFT-PBE method for ML, bilayer, and trilayer BP are about 1.01, 0.81, and 0.69 eV, respectively [34–36]. By contrast, the HSE06 bandgaps for doped ML, bilayer, and trilayer BP are 1.52, 1.01, and 0.75 eV,

respectively [37], which are apparently larger than the experimental ones. For another example, the band gap of the doped $MoSe_2$ calculated with DFT-PBE method (1.53 eV) is in accord with that calculated with the most accurate GW method (1.59 eV), and the experimental result (1.58 eV) [31].

In our study, we mainly care about whether bulk and ML InSe can conduct electrons after the absorption of Li ions. After the absorption of Li ions, InSe is highly doped by electrons. Therefore, the DFT-PBE method is good enough to estimate the electronic properties of the Li doped InSe system.

The phenomenon of semiconductor-to-metal transition in Li absorbed InSe is also reflected from the PDOS analysis (Fig. 5(b) and (e) and Fig. 6(b) and (e)). The structure of PDOS is almost maintained with just the Fermi level moving to the conduction bands. According to the PDOS, the conduction bands are mainly dominated by *p* state of the Se elements but the valence bands are mainly dominated by *s* state of the In elements for both bulk and ML InSe and also the lithiuated InSe. The differential electron density of Li absorbed bulk and ML InSe is shown in Figs. 5(f) and Fig. 6(f), respectively. There is no electron density reduction or increase in the interlayer of the two InSe sublayers (Fig. 5(c)) for pristine bulk InSe, but after the absorption of Li ions, there is electron density reduction in the interlayer around the Li-ion, and electron density increase on the top of Se-atom which is close to the Li-ion (Fig. 5(f)). There is no electron density increase in the In−Se bond direction (Fig. 6(c)) for pristine ML InSe, but after the absorption of Li ions, there is electron density increase around the Se-atom which is close to the Li-ion, and electron density decrease around the Li-ion in the In−Se bond direction (Fig. 6(f)). Apparently, Li-ion donates electrons to its adjacent Se-atom in both bulk and ML InSe systems. According to the Mulliken population analysis, the Li donates about $0.9e^-$ and $0.8e^-$ of its $2s^1$ electron to bulk and ML InSe, respectively, suggestive of a strong ionic interaction. The Mulliken population analysis shows that the bond order between Li ions and the three adjacent Se-atoms is about 0.1 in $Li_{0.25}(InSe)_2$ system for ML InSe, and the bond order between Li-ion and the Se-atom just upon the Li-ion is about 0.3 and that between the Li-ion and the other three adjacent Se-atoms under the Li-ion is also about 0.1 in $Li_{0.25}(InSe)_4$ system for bulk InSe, suggestive of a weak covalent bond between Li and Se atoms. Hence, Li ions combine InSe layer chiefly through ionic bonds, and Li exists in the cationic state on InSe layer.

2.3. Diffusion of Li ions in bulk and on ML InSe

The diffusion of Li ions in the interlayer region of bulk and ML InSe is an important factor that affects the performance of the anode. According to the Arrhenius equation [38], the temperature-dependent molecular diffusion constant (D) of Li ions follows

$$D \sim \exp\left(\frac{-E_a}{k_B T}\right)$$

where E_a and k_B are the activation energy (diffusion barrier height) and Boltzmann's constant respectively, and T the environmental temperature. Therefore, the transport properties of Li ions are mainly dependent on the Li ions diffusion barrier. According to our calculations, the migration path is $T_1 \rightarrow T_2 \rightarrow T_3$ for Li ions moving in bulk InSe and that is $H_1 \rightarrow T_{In} \rightarrow H_2$ on the surface of ML InSe along the zigzag direction, as shown in Fig. 3. In the case of Li ions diffusion in bulk InSe, the T_3 site is a symmetric site with T_1. Besides, at $x = 0.25$ and 0.167, T_2 site is another symmetric site with T_1 and T_3 because the T_2 site has the Li-ion underneath one Se-atom and upon one In-atom of the other InSe layer, the same as T_1 and T_3 which have the Li-ion underneath one In-atom and upon one Se-atom of the other InSe layer. The Li-ion is always closer to the Se-atom than to the In-atom no matter at the T_1, T_2, or T_3 sites for Li ions moving in bulk InSe because of the smaller atom diameter of the Se-atom than the In-atom, and that's why there is a very small difference between the T_1 and T_2 site (δ) in the *z* direction. Hence, all the T_1, T_2, and T_3 sites are the most stable binding site at $x = 0.25$ and 0.167. However, at $x = 0.125$ and 0.1 at the T_2 site when Li ions diffuse in bulk InSe, the Li-ion cannot get underneath a Se-atom but come to the hollow site between the two hexagonal centers. In this case, the T_2 site is an intermediate state rather than the most stable binding site. In the case of Li ions diffusion on the surface of ML InSe at all the lithium densities, H_2 site is a symmetric site with the H_1 site, and both of them are the most stable sites and the T_{In} site is an intermediate state.

The energy profiles of Li ions diffusion in bulk and ML InSe at $x = 0.25$, 0.167, 0.125, and 0.1 are depicted in Fig. 7. The T_1, T_2, and T_3 (H_1, T_{In}, and H_2) are at the bottom points along the energy profile in bulk (ML) InSe case, and S_1 and S_2 are at the peak points along the energy profile, which are the saddle points. The T_2 site has almost the same energy as the T_1 and T_3 sites at $x = 0.25$ and 0.167 while Li

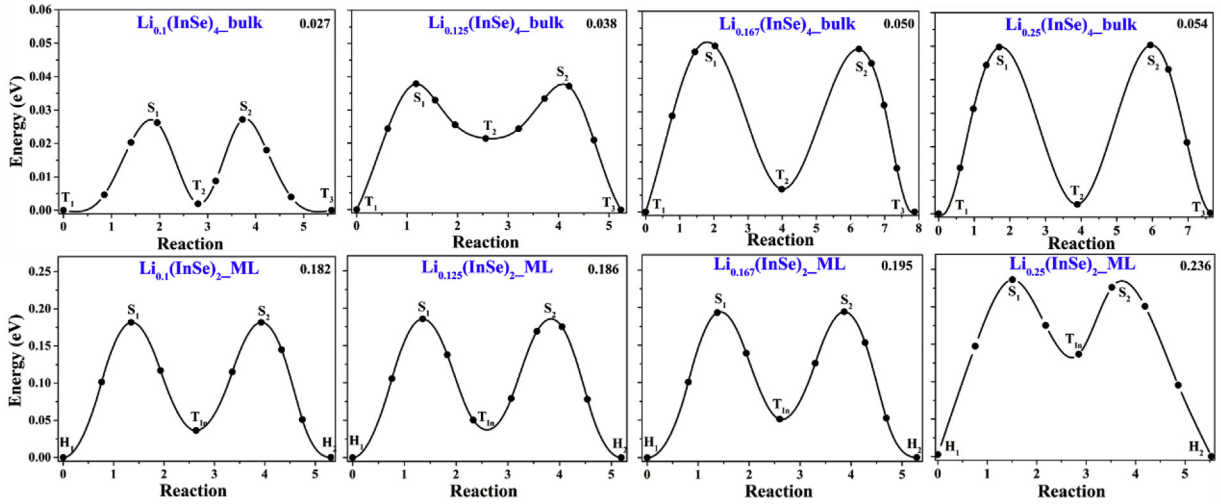

Fig. 7. Diffusion energy barrier (black solid line) of Li diffuses in bulk and on ML InSe along the reaction direction at different Li concentrations. S_1 and S_2 denote the saddle points; T_1, T_2, and T_3 (H_1, H_2, and T_{In}) denote the stable or sub-stable binding sites. The energy maximum (corresponding to the barrier value) is indicated at the top-right corner of the plot.

ions migrate in bulk InSe, indicating again that the T_2 is a symmetric site with T_1 and T_3. Although at $x = 0.1$, the energy difference between T_2 and T_1 (or T_3) is also small, the T_2 site is the hollow site rather than the T site as T_1 and T_3 as depicted in Fig. 3. So, at $x = 0.1$, the T_2 site is not a symmetric site with T_1 (or T_3).

Fig. 8 depicts the highest diffusion barrier height as the function of Li-ion density. The barrier heights for Li ions diffusion in bulk InSe range between 0.027 and 0.054 eV, and those for Li diffusion on ML InSe range between 0.182 and 0.236 eV. At any density of Li-ion, the Li ions need to overcome a smaller energy barrier in bulk InSe than on ML InSe, which means that Li ions would have much higher diffusion velocity in bulk InSe than on ML InSe surface. The diffusion barrier height monotonically increases with the increasing of Li-ion density for Li ions diffusion both in bulk and on the surface of ML InSe.

We also set the diffusion pathway along the armchair direction initially for Li ions diffusion both in bulk InSe and on ML InSe as shown in Fig. S5 (dark imaginary arrows), and the Li ions finally go from the initial site through the zigzag direction and get to the final site as shown in Fig. S5 (red solid arrows). Such a phenomenon suggests that Li ions can only diffuse along the zigzag direction in both bulk and ML InSe.

The diffusion barriers heights for Li ions diffusion in bulk and ML InSe are remarkably small compared with those of Li ions migration in many other anode materials. For example, the theoretical diffusion barrier heights are about 0.22 and 0.38 eV for Li ions diffusion in graphite and on graphene, respectively, and graphite has also been used as commercialized anode material presently [25,29,39,40]. For another example, the theoretical diffusion barrier heights on ML MoS_2, VS_2, and silicene are 0.21, 0.22, and 0.23 eV respectively [5,29,41], and the diffusion barrier height in bulk MoS_2 is 0.49 eV, which are all much larger than those in InSe. All these example data are calculated at the Li-ion density where the distance between Li ions is beyond the scope of Li ions interaction. According to the Arrhenius equation, the Li diffusion constant in the bulk InSe is estimated to be about 7×10^2 and 2×10^7 times as fast as that in graphite and bulk MoS_2, respectively [5,25]. The Li diffusion constant on ML InSe is about 3×10^2 times as fast as that on graphene [39]. The Li diffusion constant in bulk InSe would be around 10^2 times as fast as that for Li ions on ML InSe at room temperature. The small diffusion barrier height for Li diffusion in the layered bulk InSe guarantees a very fast diffusion rate and also a very high rate capability.

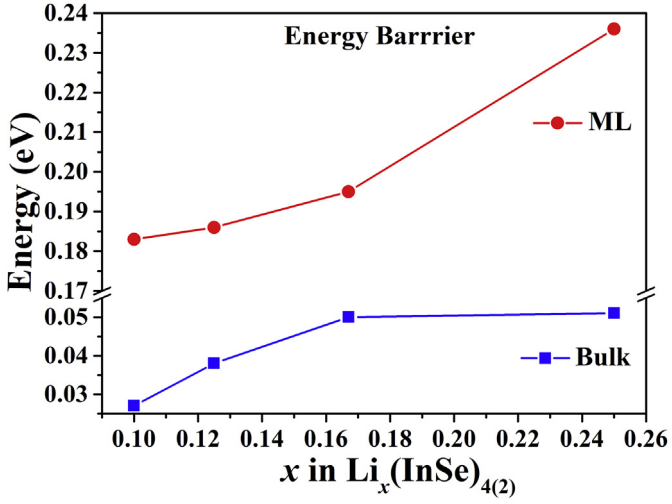

Fig. 8. Diffusion barrier height as a function of Li density x for bulk (black) and ML (red) InSe, $Li_x(InSe)_{4(2)}$. (For interpretation of the references to colour in this figure legend, the reader is referred to the Web version of this article.)

3. Conclusion

The groove structure of layered materials is a favorable character helping materials to possess a low Li-ion diffusion batter height. The diffusion barrier heights for Li ions migration in InSe, which has the groove character, range in 0.027–0.054 eV (bulk InSe), and 0.182–0.236 eV (ML InSe). Such diffusion barrier heights are quiet low compared with other electrode materials. Besides, we firstly find that the diffusion barrier heights are monotonically decreased as the Li-ion density increases. The Li ions are able to form stable absorption with both bulk and ML InSe with the binding energy ranging from −0.62 to −1.61 eV and form −0.43 to −0.96 eV for bulk and ML InSe, respectively, and the binding energies are nearly monotonically increased as the density of Li-ion increases.

Acknowledgment

This work was supported by the National Natural Science Foundation of China (Nos. 11674005, 11664026, and 11704406), Ministry of Science and Technology of China (Nos. 2016YFB0700600 (National Materials Genome Project) and 2016YFA0301300).

Appendix A. Supplementary data

Supplementary data to this article can be found online at https://doi.org/10.1016/j.cocom.2019.e00404.

References

[1] W. Li, Y. Yang, G. Zhang, Y.W. Zhang, Ultrafast and directional diffusion of lithium in phosphorene for high-performance lithium-ion battery, Nano Lett. 15 (2015) 1691–1697.
[2] B. Mortazavi, A. Dianat, O. Rahaman, G. Cuniberti, T. Rabczuk, Borophene as an anode material for Ca, Mg, Na or Li ion storage: a first-principle study, J. Power Sources 329 (2016) 456–461.
[3] D.G. Ladha, A review on density functional theory–based study on two-dimensional materials used in batteries, Mater. Today Chem. 11 (2019) 94–111.
[4] Q. Tang, Z. Zhou, P. Shen, Are MXenes promising anode materials for Li ion batteries? Computational studies on electronic properties and Li storage capability of Ti_3C_2 and $Ti_3C_2X_2$ (X = F, OH) monolayer, J. Am. Chem. Soc. 134 (2012) 16909–16916.
[5] Y. Li, D. Wu, Z. Zhou, C.R. Cabrera, Z. Chen, Enhanced Li adsorption and diffusion on MoS_2 zigzag nanoribbons by edge effects: a computational study, J. Phys. Chem. Lett. 3 (2012) 2221–2227.
[6] W. Li, Y. Yang, G. Zhang, Y.-W. Zhang, Ultrafast and directional diffusion of lithium in phosphorene for high-performance lithium-ion battery, Nano Lett. 15 (2015) 1691–1697.
[7] D.A. Bandurin, A.V. Tyurnina, G.L. Yu, A. Mishchenko, V. Zólyomi, S.V. Morozov, R.K. Kumar, R.V. Gorbachev, Z.R. Kudrynskyi, S. Pezzini, Z.D. Kovalyuk, U. Zeitler, K.S. Novoselov, A. Patanè, L. Eaves, I.V. Grigorieva, V.I. Fal'ko, A.K. Geim, Y. Cao, High electron mobility, quantum Hall effect and anomalous optical response in atomically thin InSe, Nat. Nanotechnol. 12 (2017) 223–227.
[8] M. Millot, J.-M. Broto, S. George, J. González, A. Segura, Electronic structure of indium selenide probed by magnetoabsorption spectroscopy under high pressure, Phys. Rev. B 81 (2010) 205211.
[9] W. Feng, W. Zheng, W. Cao, P. Hu, Back gated multilayer InSe transistors with enhanced carrier mobilities via the suppression of carrier scattering from a dielectric interface, Adv. Mater. 26 (2014) 6587–6593.
[10] W. Feng, X. Zhou, W.Q. Tian, W. Zheng, P. Hu, Performance improvement of multilayer InSe transistors with optimized metal contacts, Phys. Chem. Chem. Phys. 17 (2015) 3653–3658.
[11] Z. Yang, W. Jie, C.-H. Mak, S. Lin, H. Lin, X. Yang, F. Yan, S.P. Lau, J. Hao, Wafer-scale synthesis of high-quality semiconducting two-dimensional layered InSe with broadband photoresponse, ACS Nano 11 (2017) 4225–4236.
[12] X. Li, C. Xia, X. Song, J. Du, W. Xiong, *n*- and *p*-type dopants in the InSe monolayer via substitutional doping, J. Mater. Sci. 52 (2017) 7207–7214.
[13] P.H. Ho, Y.R. Chang, Y.C. Chu, M.K. Li, C.A. Tsai, W.H. Wang, C.H. Ho, C.W. Chen, P.W. Chiu, High-mobility InSe transistors: the role of surface oxides, ACS Nano 11 (2017) 7362–7370.
[14] G.W. Mudd, S.A. Svatek, T. Ren, A. Patane, O. Makarovsky, L. Eaves, P.H. Beton,

Z.D. Kovalyuk, G.V. Lashkarev, Z.R. Kudrynskyi, A.I. Dmitriev, Tuning the bandgap of exfoliated InSe nanosheets by quantum confinement, Adv. Mater. 25 (2013) 5714–5718.
[15] S. Lei, L. Ge, S. Najmaei, A. George, R. Kappera, J. Lou, M. Chhowalla, H. Yamaguchi, G. Gupta, R. Vajtai, A.D. Mohite, P.M. Ajayan, Evolution of the electronic band structure and efficient photo-detection in atomic layers of InSe, ACS Nano 8 (2014) 1263–1272.
[16] S.R. Tamalampudi, Y.-Y. Lu, R.U. Kumar, R. Sankar, C.-D. Liao, K.B. Moorthy, C.-H. Cheng, F.C. Chou, Y.-T. Chen, High performance and bendable few-layered InSe photodetectors with broad spectral response, Nano Lett. 14 (2014) 2800–2806.
[17] W. Feng, J.-B. Wu, X. Li, W. Zheng, X. Zhou, K. Xiao, W. Cao, B. Yang, J.-C. Idrobo, L. Basile, W. Tian, P. Tan, P. Hu, Ultrahigh photo-responsivity and detectivity in multilayer InSe nanosheets phototransistors with broadband response, J. Mater. Chem. C 3 (2015) 7022–7028.
[18] G.W. Mudd, S.A. Svatek, L. Hague, O. Makarovsky, Z.R. Kudrynskyi, C.J. Mellor, P.H. Beton, L. Eaves, K.S. Novoselov, Z.D. Kovalyuk, E.E. Vdovin, A.J. Marsden, N.R. Wilson, A. Patane, High broad-band photoresponsivity of mechanically formed InSe-graphene van der Waals heterostructures, Adv. Mater. 27 (2015) 3760–3766.
[19] H.R. Jiang, Z. Lu, M.C. Wu, F. Ciucci, T.S. Zhao, Borophene: a promising anode material offering high specific capacity and high rate capability for lithium-ion batteries, Nanomater. Energy 23 (2016) 97–104.
[20] M. Brandbyge, J.L. Mozos, P. Ordejon, J. Taylor, K. Stokbro, Density-functional method for nonequilibrium electron transport, Phys. Rev. B 65 (2002) 165401.
[21] J.P. Perdew, K. Burke, M. Ernzerhof, Generalized gradient approximation made simple, Phys. Rev. Lett. 77 (1996) 3865–3868.
[22] H.J. Monkhorst, J.D. Pack, Special points for brillouin-zone integrations, Phys. Rev. B 13 (1976) 5188–5192.
[23] G. Henkelman, H. Jónsson, Improved tangent estimate in the nudged elastic band method for finding minimum energy paths and saddle points, J. Chem. Phys. 113 (2000) 9978–9985.
[24] G. Henkelman, B.P. Uberuaga, H. Jónsson, A climbing image nudged elastic band method for finding saddle points and minimum energy paths, J. Chem. Phys. 113 (2000) 9901–9904.
[25] K. Persson, Y. Hinuma, Y.S. Meng, A. Van Der Ven, G. Ceder, Thermodynamic and kinetic properties of the Li-graphite system from first-principles calculations, Phys. Rev. B 82 (2010) 125416.
[26] E. Lee, K.A. Persson, Li absorption and intercalation in single layer graphene and few layer graphene by first principles, Nano Lett. 12 (2012) 4624–4628.
[27] H.R. Jiang, T.S. Zhao, M. Liu, M.C. Wu, X.H. Yan, Two-dimensional SiS as a potential anode material for lithium-based batteries: a first-principles study, J. Power Sources 331 (2016) 391–399.
[28] Q. Kong, W. Feng, Q. Wang, L.Y. Gan, C. Sun, SiS nanosheets as a promising anode material for Li-ion batteries: a computational study, Phys. Chem. Chem. Phys. 19 (2017) 8563–8567.
[29] Y. Jing, Z. Zhou, C.R. Cabrera, Z. Chen, Metallic VS_2 monolayer: a promising 2D anode material for lithium ion batteries, J. Phys. Chem. C 117 (2013) 25409–25413.
[30] S. Demirci, N. Avazlı, E. Durgun, S. Cahangirov, Structural and electronic properties of monolayer group III monochalcogenides, Phys. Rev. B 95 (2017) 115409.
[31] Y. Liang, L. Yang, Carrier plasmon induced nonlinear band gap renormalization in two-dimensional semiconductors, Phys. Rev. Lett. 114 (2015) 063001.
[32] Y. Wang, P. Huang, M. Ye, R. Quhe, Y. Pan, H. Zhang, H. Zhong, J. Shi, J. Lu, Many-body effect, carrier mobility, and device performance of hexagonal arsenene and antimonene, Chem. Mater. 29 (2017) 2191–2201.
[33] S. Das, W. Zhang, M. Demarteau, A. Hoffmann, M. Dubey, A. Roelofs, Tunable transport gap in phosphorene, Nano Lett. 14 (2014) 5733–5739.
[34] X. Zhang, Y. Pan, M. Ye, R. Quhe, Y. Wang, Y. Guo, H. Zhang, Y. Dan, Z. Song, J. Li, J. Yang, W. Guo, J. Lu, Three-layer phosphorene-metal interfaces, Nano Res. 11 (2018) 707–721.
[35] Y. Pan, Y. Wang, M. Ye, R. Quhe, H. Zhong, Z. Song, X. Peng, D. Yu, J. Yang, J. Shi, J. Lu, Monolayer phosphorene-metal contacts, Chem. Mater. 28 (2016) 2100–2109.
[36] Y. Pan, Y. Dan, Y. Wang, M. Ye, H. Zhang, R. Quhe, X. Zhang, J. Li, W. Guo, L. Yang, J. Lu, Schottky barriers in bilayer phosphorene transistors, ACS Appl. Mater. Interfaces 9 (2017) 12694–12705.
[37] Y. Cai, G. Zhang, Y.W. Zhang, Layer-dependent band alignment and work function of few-layer phosphorene, Sci. Rep. 4 (2014) 6677.
[38] W. Li, Y. Mu, Dissociation of hydrophobic and charged nano particles in aqueous guanidinium chloride and urea solutions: a molecular dynamics study, Nanoscale 4 (2012) 1154–1159.
[39] C. Uthaisar, V. Barone, Edge effects on the characteristics of Li diffusion in graphene, Nano Lett. 10 (2010) 2838–2842.
[40] E. Yoo, J. Kim, E. Hosono, H.S. Zhou, T. Kudo, I. Honma, Large reversible Li storage of graphene nanosheet families for use in rechargeable lithium ion batteries, Nano Lett. 8 (2008) 2277–2282.
[41] G.A. Tritsaris, E. Kaxiras, S. Meng, E. Wang, Adsorption and diffusion of lithium on layered silicon for Li-ion storage, Nano Lett. 13 (2013) 2258–2263.

Update

Computational Condensed Matter

Volume 27, Issue , June 2021, Page

DOI: https://doi.org/10.1016/j.cocom.2021.e00545

Computational Condensed Matter 27 (2021) e00545

Contents lists available at ScienceDirect

Computational Condensed Matter

journal homepage: http://ees.elsevier.com/cocom/default.asp

Erratum regarding missing Declaration of Competing Interest statements in previously published articles

Declaration of Competing Interest statements were not included in published version of the articles that appeared in previous volumes of Computational Condensed Matter.

Please see the appropriate Declaration of Competing Interest statements below.

S.No	Article Title	Journal Title	Year	Volume	Item/Article Number
1	Magnetic properties of a mixed spin Ising nanowire with inner core, inter core-shell and outer shell morphology	Computational Condensed Matter	2018	16C	297
2	Band-gap modulation of carbon nanotubes with Haeckelite structure under a transverse electric field: A first principle study	Computational Condensed Matter	2018	15C	144
3	Electronic and optical properties of SrS nanosheet in 001 and 101 directions	Computational Condensed Matter	2019	22C	445
4	Investigation of high figure of merit in semiconductor XHfGe (XÂ = Â NiÂ and Pd) half-Heusler alloys: Ab-initio study	Computational Condensed Matter	2019	21C	407
5	Absorption and diffusion of lithium on layered InSe	Computational Condensed Matter	2019	21C	404
6	Electronic structure, chemical bonding, optical, elastic and dynamical properties of MeB2 compounds: Effect of transition metal Meâ€ = â€Sc, Ti and Zr	Computational Condensed Matter	2019	21C	406
7	Stability of intrinsic and extrinsic co-decorated boron sheets with Li and Mg	Computational Condensed Matter	2018	17C	345
8	First-principles study of half-metallic properties in X2VSi (XÂ = Ti, Co) and their quaternary TiCoVSi and CoTiVSi compounds	Computational Condensed Matter	2019	19C	369
9	The effects of vanadium absorbed by WS2 monolayer on the electronic, magnetic and optical properties: A first principle study	Computational Condensed Matter	2018	18C	352
10	Photoferroelectricity in di-phenylalanine peptide nanotubes	Computational Condensed Matter	2018	14C	124
11	Electronic properties of silicon carbide nanotube with Stone Wales defects under uniaxial pressure: A computational study	Computational Condensed Matter	2019	19C	378
12	Tuning the electronic structure and magnetic coupling in armchair B2S nanoribbons using strain and staggered sublattice potential	Computational Condensed Matter	2019	21C	424
13	Ferromagnetism induced by Cr, V single and double impurities doped BN from Ab-initio and Monte Carlo study	Computational Condensed Matter	2018	16C	317
14	First principles investigation of magnetic new carbon-rich layered compounds UCn (n = 2, 6, 12)	Computational Condensed Matter	2019	21C	397
15	Study of the linear and nonlinear response properties of the zinc-blende AlP, GaP and their AlxGa1-xP ternary alloys using first principle calculations	Computational Condensed Matter	2019	21C	410

The authors were contacted after publication to request a Declaration of Interest statement.

The authors declare that they have no known competing financial interests or personal relationships that could have appeared to influence the work reported in this paper.

DOIs of original article: https://doi.org/10.1016/j.cocom.2019.e00404, https://doi.org/10.1016/j.cocom.2019.e00410, https://doi.org/10.1016/j.cocom.2018.e00297, https://doi.org/10.1016/j.cocom.2018.03.005, https://doi.org/10.1016/j.cocom.2019.e00406, https://doi.org/10.1016/j.cocom.2018.e00345, https://doi.org/10.1016/j.cocom.2019.e00378, https://doi.org/10.1016/j.cocom.2019.e00407, https://doi.org/10.1016/j.cocom.2018.e00352, https://doi.org/10.1016/j.cocom.2018.e00317, https://doi.org/10.1016/j.cocom.2019.e00397, https://doi.org/10.1016/j.cocom.2019.e00445, https://doi.org/10.1016/j.cocom.2019.e00424, https://doi.org/10.1016/j.cocom.2019.e00369, https://doi.org/10.1016/j.cocom.2017.11.007.

https://doi.org/10.1016/j.cocom.2021.e00545